

Modelling the angle-dependent magnetoresistance oscillations of Fermi surfaces with hexagonal symmetry

Joseph C. A. Prentice^{1,2} and Amalia I. Coldea¹

¹*Clarendon Laboratory, Department of Physics, University of Oxford, Parks Road, Oxford, OX1 3PU, U.K.*

²*TCM Group, Cavendish Laboratory, University of Cambridge, J. J. Thomson Avenue, Cambridge, CB3 0HE, U.K.*

By solving the Boltzmann transport equation we investigate theoretically the general form of oscillations in the resistivity caused by varying the direction of an applied magnetic field for the case of quasi-two dimensional systems on hexagonal lattices. The presence of the angular magnetoresistance oscillations can be used to map out the topology of the Fermi surface and we study how this effect varies as a function of the degree of inter-plane warping as well as a function of the degree of isotropic scattering. We find that the angular dependent effect due to in-plane rotation follows the symmetry imposed by the lattice whereas for inter-plane rotation the degree of warping dictates the dominant features observed in simulations. Our calculations make predictions for specific angle-dependent magnetotransport signatures in magnetic fields expected for quasi-two dimensional hexagonal compounds similar to PdCoO₂ and PtCoO₂.

I. INTRODUCTION

The electronic and thermal properties of exotic metals and superconductors originate from the intricate details of their Fermi surfaces. Understanding the Fermi surface of a material requires direct experimental measurements through various techniques, such as angle-resolved photoemission spectroscopy (ARPES)¹ and quantum oscillations experiments by measuring the de Haas-van Alphen (dHvA) and/or Shubnikov-de Haas (SdH) effects². Another powerful method of understanding the shape of simple Fermi surfaces is angle-dependent magnetoresistance oscillations (AMRO), which allow access to the Fermi surface at much higher temperatures and scattering rates than the purely quantum oscillation effects. This method has been employed successfully to map both quasi-one dimensional (Q1D) and quasi-two dimensional (Q2D) Fermi surfaces, as in BEDT-TTF organic salts^{3,4}, intercalated graphite compounds⁵, ruthenates⁶, and superconducting pnictides⁷ and cuprates⁸⁻¹⁴.

Many electronic systems with hexagonal symmetry possess interesting transport properties, such as unusual anisotropy in electronic scattering, charge-density waves phenomena and backscattering protected transport on the surface of topological insulators. PdCoO₂ is one such interesting material, belonging to a more general family of delafossite compounds, which has been found to have extremely large magnetoresistance¹⁵ and unusual transport properties¹⁶, with strong transport anisotropy between the in-plane and out-of-plane directions, which differ by a factor of up to 200¹⁷. Recent experimental angle-dependent studies show very strong features in the magnetoresistance of PdCoO₂, both when the magnetic field is rotated in the conductive plane¹⁵ as well as out-of-plane¹⁸. Furthermore, quantum oscillations show that the data can be modelled using a single corrugated hexagonal Fermi surface¹⁹.

In this work, we use the Boltzmann equation²⁰ to calculate the angle dependent magnetotransport properties for electronic systems with hexagonal symmetry, which have not been explored before. Starting from a tight-binding description of

the Fermi surface on a hexagonal lattice, we investigate the angle dependent magnetoresistance when the magnetic field is rotated, either in the conducting plane or out-of-plane, focusing in particular on the role of scattering and the degree of warping of the Fermi surface. We find that the form of the magnetoresistance depends strongly on the degree of warping, with additional features emerging at high warping levels. Our work provides a large range of parameters that can be used to compare with future experimental studies for materials with a single quasi-two dimensional hexagonal Fermi surface, such as PdCoO₂ and PtCoO₂.

II. FERMION SURFACE HARMONIC EXPANSION

In order to investigate analytically a single Fermi surface on a hexagonal lattice we used a tight-binding approach to expand a quasi-two dimensional Fermi surface using cylindrical harmonics, as considered in previous studies^{6,10,19}:

$$k_F(\psi, k_z) = \sum_{m,n \geq 0} k_{n,m} \begin{Bmatrix} \cos \\ \sin \end{Bmatrix} m\psi \times \begin{Bmatrix} \cos \\ \sin \end{Bmatrix} n\kappa \quad (1)$$

where $\kappa = dk_z = \frac{ck_z}{3}$, d is the spacing between conducting layers and ψ is the azimuthal angle in the cylindrical coordinate system used. $\kappa \in [-\pi, \pi]$. k_{00} gives the average radius of the FS, whilst the other coefficients give various corrugations and warpings of the surface, as shown in Fig. 1. This expansion must obey the symmetries of the hexagonal lattice as identified by the following symmetry operations:

1. Rotation and translation: $\psi \rightarrow \psi + \frac{\pi}{3}, \kappa \rightarrow \kappa + \pi$
2. Rotation: $\psi \rightarrow \psi + \frac{2\pi}{3}$
3. Inversion: $\psi \rightarrow \psi + \pi, \kappa \rightarrow -\kappa$
4. Reflection 1: $\psi \rightarrow -\psi$
5. Reflection 2: $\psi \rightarrow \frac{2\pi}{3} - \psi$

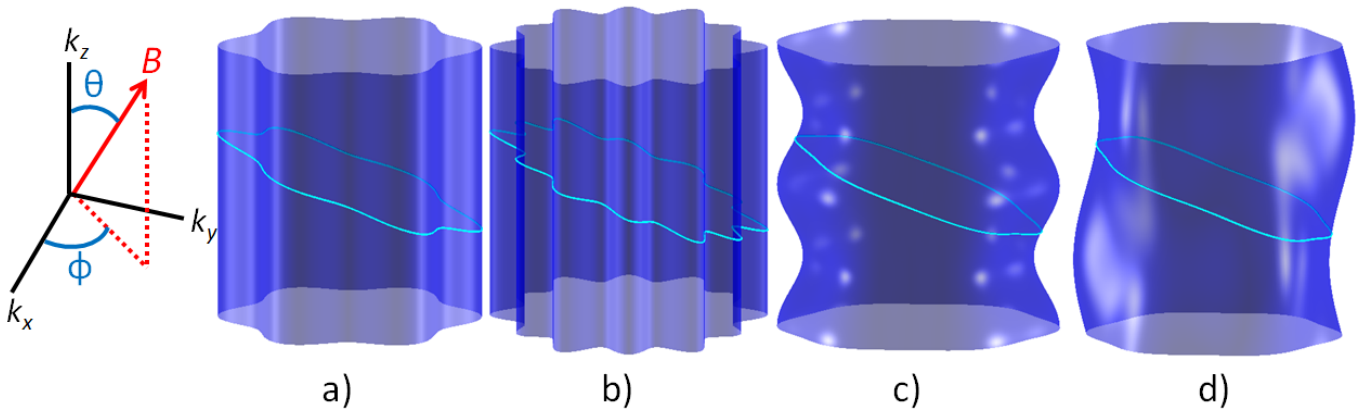


FIG. 1. (colour online) Simulated hexagonal Fermi surfaces. The effect of different anisotropic terms defined in Eq. (2) and set as $k_{00}=0.9559$ throughout and a) $k_{0,6}=0.1$, b) $k_{0,12}=0.1$ and $k_{0,6}=0.04$, c) $k_{2,0}=0.1$ and $k_{0,6}=0.04$ and d) $k_{1,3}=0.1$ and $k_{0,6}=0.04$, all parameters in units of \AA^{-1} . Solid line indicates a typical cyclotron orbit for a particular Fermi surface when the applied magnetic field makes the polar angle, θ , and azimuthal angle, ϕ , with respect to the direction of the magnetic field \mathbf{B} , as shown in the left panel.

suggesting that m and n must both be odd or both be even based on 1), $m \bmod 3 = 0$ based on 2), $\cos n\kappa$ terms must be accompanied by even m and $\sin n\kappa$ terms must be accompanied by odd m based on 3), and only $\cos m\psi$ terms are allowed based on 4) and 5). These operations are discussed in more detail in Appendix J. Taking all these constraints and assuming that near-neighbour hopping dominates by ignoring higher order terms of the expansion²¹, we are left with the expression:

$$k_F = k_{00} + k_{0,6} \cos 6\psi + k_{0,12} \cos 12\psi + k_{2,0} \cos 2\kappa + k_{1,3} \sin \kappa \cos 3\psi. \quad (2)$$

Fig.1 shows this for different values of the coefficients. This expression is similar to that reported in Ref. 19, except the additional term, $k_{0,1}$, which is ruled out by the first symmetry operation. Physically, the $k_{2,0}$ and $k_{1,3}$ terms are related to interlayer anisotropy of the Fermi surface, whilst the other terms are related to in-plane anisotropy. The effect of each of these anisotropic terms on the shape of the Fermi surface is shown in Fig. 1, where $k_{0,6}$ introduces a 6-fold symmetry whilst $k_{0,12}$ introduces a 12-fold symmetry, and $k_{2,0}$ and $k_{1,3}$ terms introduce warping in the k_z -direction. In this work $k_{1,3}$ will be used as a variable to investigate the effect of FS warping on AMRO and the values of the parameters are chosen to be $k_{00} = 0.9559$, $k_{0,6} = 0.04$, $k_{0,12} = 0.007$ and $k_{2,0} = -0.0025$ (in units of \AA^{-1}) taken to match closely the experimental values for PdCoO₂, as determined from quantum oscillations¹⁹. We choose $k_{1,3}$ as our variable parameter because we expect it will give a rich structure to the resulting AMRO - as we are calculating the c -axis resistivity, we would expect terms containing k_z dependence to have the largest effect on the AMRO. Using $k_{1,3}$ as a variable allows us to explore a range of plausible AMRO resulting from warped PdCoO₂-like Fermi surfaces, whereas using other parameters from the expansion would affect the AMRO in a more subtle way.

These parameters can be directly related to the transfer integrals in a usual tight-binding model as detailed in Refs. 15 and

19 and discussed in Appendix I. However, when directly inferring the tight-binding overlap integrals from quantum oscillation experiments there are certain limitations - the bare electronic bandwidth is inaccessible by these experiments, and only the states near the Fermi surface are probed, meaning one can determine the Fermi surface geometry and the renormalized bandwidth. The energy bands and the transfer integrals lose their meaning away from the Fermi surface in a strongly interacting system. Thus, the use of a cylindrical harmonic expansion allows us to parametrize the Fermi surface geometry directly from the electronic structure information obtained from experimental data, in particular when comparing quantum oscillations and AMRO data.

In order to numerically calculate the AMRO, for fields both in and out of the (ab) -plane, we calculate the conductivity, and thus ρ_{zz} , for a certain FS of the form in Eq. (2), using MATLAB²². In order to calculate the AMRO in this work, we calculated ρ_{zz} simply by taking $\rho_{zz} = \frac{1}{\sigma_{zz}}$, similar to previous work¹⁰. This expression follows from the fact that off-diagonal terms in the conductivity matrix are generally much smaller than the diagonal ones, as they directly depend on the warping of the Fermi surface, and those off-diagonal elements containing a z -component are even smaller, as $v_z \ll v_x, v_y$, as shown in Appendix E. Results using this expression agree well with further calculations done using the more exact method of calculating and inverting the whole conductivity matrix to obtain ρ_{zz} , as shown in Fig. 6 in Appendix F, and were also less prone to numerical errors.

Throughout this work, anisotropy in the effective mass of the electrons and the scattering time is neglected, with the values of the isotropic scattering time taken as $\tau = 10$ ps and the quasiparticle effective mass as $m^* = 1.5m_e$ (after Refs. 15 and 19). Previous calculations of AMRO without the inclusion of anisotropy in τ and $\omega_c = \frac{eB}{m^*}$ have also been shown to reproduce the key features of the AMRO seen in experiments, such as in previous work on quasi-two-dimensional cuprates⁹. The AMRO features are captured qualitatively by the isotropic calculations, with differences starting to emerge

at large θ angles²³. This implies that we can draw valid conclusions from calculations that do not include anisotropy in the scattering time or effective mass. This conclusion is also justified by experiments on PdCoO₂ up to 100 K, which are described by a single isotropic scattering rate¹⁵, implying that impurity scattering is the dominant process in the regime in which AMRO are observed. In general, anisotropy in the effective mass, and thus the cyclotron frequency ω_c , arises via the expression $\frac{\mathbf{k}_F \cdot \mathbf{v}_F}{k_F^2}$, where \mathbf{k}_F points along the cylindrical radial direction²³. Anisotropy arises if the two vectors are not parallel. From the results shown in Appendix E, the angle between \mathbf{k}_F and \mathbf{v}_F will be $\arctan \sqrt{\left(\frac{1}{k_F} \frac{\partial k_F}{\partial \psi}\right)^2 + \left(\frac{\partial k_F}{\partial k_z}\right)^2}$, and thus the dot product will be proportional to the cosine of this quantity. As the argument of the inverse tangent is small, we can expand the cosine as $1 - \left(\frac{1}{k_F} \frac{\partial k_F}{\partial \psi}\right)^2 - \left(\frac{\partial k_F}{\partial k_z}\right)^2$, meaning the anisotropy in m^* and ω_c is small, and will be a second order effect at best, justifying its neglect. Anisotropies in the scattering time or effective mass may introduce important quantitative corrections to our results¹⁰, but this is beyond the scope of the current work.

The oscillations in AMRO are semi-classical in nature, and are due to the formation of cyclotron orbits on the FS and the changing area enclosed by them²⁴. AMRO can be calculated from a linearised Boltzmann transport equation²⁰, which is derived in full in Appendix A. In order to calculate the magnetoresistance and thus observe AMRO, we must derive an expression for the conductivity tensor for the FS given by Eq. (2). We used the Boltzmann equation:

$$e\mathbf{E} \cdot \mathbf{v} \left(-\frac{\partial f_{\mathbf{k}}^0}{\partial \varepsilon} \right) = \frac{g_{\mathbf{k}}}{\tau} + \frac{e}{\hbar} (\mathbf{v} \times \mathbf{B}) \frac{\partial g_{\mathbf{k}}}{\partial \mathbf{k}} \quad (3)$$

where $f_{\mathbf{k}}^0$ is the particle distribution in the absence of fields or temperature gradients, $g_{\mathbf{k}}$ is the difference between the steady state distribution and $f_{\mathbf{k}}^0$ (assumed to be small), \mathbf{v} is the velocity of the particles and τ is the scattering time. Solving this equation and using it to calculate the conductivity produces the Shockley-Chambers tube integral^{25,26}:

$$\sigma_{ij} = \frac{e^2}{4\pi^3 \hbar^2} \int dk_B \int_0^{2\pi} d\alpha \int_0^\infty d\alpha'' v_i(\alpha) v_j(\alpha - \alpha'') \frac{m^*}{\omega_c} e^{-\frac{\alpha''}{\omega_c \tau}}. \quad (4)$$

This is derived in detail, in the case of closed orbits only, in the Appendices.

A generalised version of the Shockley-Chambers tube integral that includes the effect of open orbits is^{10,27}

$$\sigma_{ij} = \frac{e^2}{4\pi^3} \int d^3\mathbf{k} \left(-\frac{\partial f_{\mathbf{k}}^0}{\partial \varepsilon} \right) v_i(\mathbf{k}, 0) \int_{-\infty}^0 v_j(\mathbf{k}, t) e^{\frac{t}{\tau}} dt. \quad (5)$$

The time integral integrates over the history of the open orbit. Here we consider two cases: when the magnetic field is within the (ab) -plane ($|\theta| = 90^\circ$) and the contribution from the open orbits is dominant, or when the field is away from the (ab) -plane ($|\theta| \leq 70^\circ$) and the closed orbits dominate.

The Shockley-Chambers tube integral gives us an expression for the conductivity tensor, σ_{ij} , in terms of k_F and related quantities such as v_F and v_z . However, such an expression does not explicitly show that the magnetoresistance is oscillatory as the direction of the magnetic field varies. However, previous work^{24,28,29} has shown that, in the limit of $td \tan \theta \ll \hbar v_F$, where t is the interlayer transfer integral and $d = \frac{c}{3}$, this behaviour is general and allows us to find an expression for the positions of the peaks in the magnetoresistance⁴. For a simple cylindrical Fermi surface with no in-plane warping, the inter-plane component of the conductivity, σ_{zz} takes the form^{28,29}

$$\frac{\sigma_{zz}(\theta)}{\sigma_{zz}(0)} = [J_0(\mu)]^2 + 2 \sum_{\nu=1}^{\infty} \frac{[J_\nu(\mu)]^2}{1 + (\nu \omega_c \tau \cos \theta)^2}. \quad (6)$$

$\mu = dk_{\parallel} \tan \theta$, where k_{\parallel} is the maximum possible projection of an in-plane Fermi wavevector onto the plane of rotation. $J_\nu(\mu)$ is the ν^{th} order Bessel function of the first kind. This equation still holds approximately for low levels of Fermi surface warping²⁹, as in the current work. The oscillatory nature of the Bessel functions leads to oscillations in the magnetoresistance. In order to link these oscillations to the form of the FS, we make two assumptions: firstly that $\omega_c \tau \cos \theta$ is large enough to neglect all terms in the sum except $J_0(\mu)$, and secondly that $\mu \gg 1$ so that we can expand $J_0(\mu)$, in order to obtain expressions for the zeros of $\frac{\sigma_{zz}(\theta)}{\sigma_{zz}(0)}$. These zeros are at $\mu = n\pi + \frac{\pi}{2} \pm \frac{\pi}{4}$, where the positive sign is for $\mu < 0$ and the negative for $\mu > 0$, known as the Yamaji angles^{12,24}, allowing us to directly link the positions of AMRO peaks to the form of the FS. The first approximation will break down for θ approaching 90° , whilst the second will break down if θ becomes too small.

III. RESULTS

A. The angular magnetoresistance oscillations due to in-plane rotation

We now present the results of our AMRO simulations obtained when the magnetic field is rotated in the (ab) -plane as a function of the azimuthal angle, ϕ , for different parameters, as shown in Fig. 2. First of all, the AMRO spectra have a 60° periodicity in ϕ , as would be expected from the hexagonal symmetry, and the AMRO peaks become sharper and more prominent as the degree of the inter-plane c -axis warping, $k_{1,3}$, increases (see Fig. 2a). This variation can be quantified by the variation of its full width at half maximum w , as a function of $k_{1,3}$ which clearly shows an exponential decay as the peaks become sharper and sharper (see Fig. 2d). This could potentially be caused by how the integral for σ_{zz} contains a factor of $\frac{1}{k_F}$ - for low levels of c -axis warping, the value of k_F decreases almost linearly as we move away from the corners of the hexagonal prism, whilst for high levels of warping, k_F decreases more quickly as we move away from the corners. This means that $\frac{\Delta \rho}{\rho} \propto \frac{1}{\sigma_{zz}}$ will behave similarly, leading to the width of the peaks reducing as warping increases.

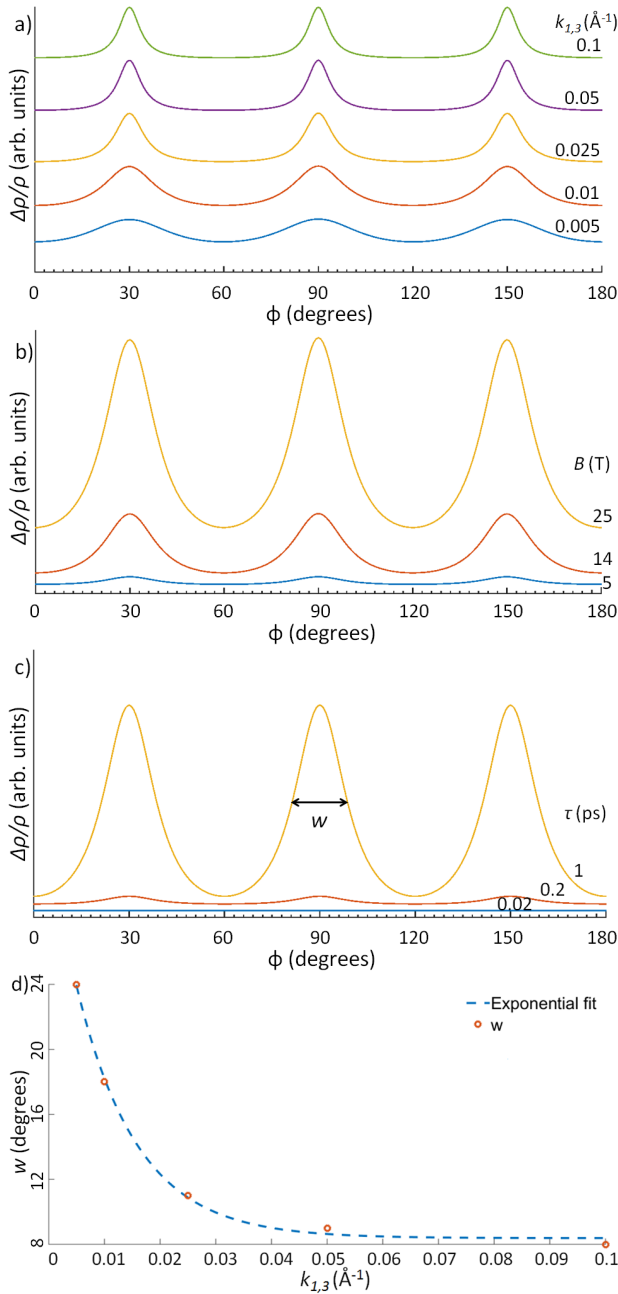


FIG. 2. (colour online) Simulated AMROs as a function of azimuthal angle, ϕ , for different values of a) the c -axis warping $k_{1,3} = 0.005 - 0.1 \text{ \AA}^{-1}$, b) the magnetic field strength, $B = 5 - 25 \text{ T}$, and c) the isotropic scattering time, $\tau = 0.02 - 1 \text{ ps}$. Each set of AMRO is normalised by the range of $\frac{\Delta\rho}{\rho}$ values within the set and shifted vertically for clarity, and the constant parameters used in simulations were $k_{1,3} = 0.01 \text{ \AA}^{-1}$, $\tau = 10 \text{ ps}$, $m^* = 1.5m_e$ and $B = 25 \text{ T}$. The exponential effect of warping $k_{1,3}$ on the full width at half maximum of the peaks, w , (defined in c) is shown in d). Dashed line is an exponential fit of the form $w = ae^{-bk_{1,3}} + c$ with $a = 24.493^\circ$, $b = 91.346 \text{ \AA}$, and $c = 8.3818^\circ$.

Next, we investigate the effect of the magnetic field strength, B , and isotropic scattering time, τ , on the in-plane AMRO as a function of the azimuthal angle, ϕ . We observe a continuous enhancement of magnetoresistance as a function of both B and τ , as shown in Fig. 2b) and c). The quantity $\omega_c\tau = \frac{eB\tau}{m^*}$ dictates how far a quasiparticle travels before scattering, as can be seen in the exponential within the integrand of Eq. (4), and thus controls its contribution to the integral giving σ_{zz} . At the minima of the in-plane AMRO, v_z is essentially zero, making σ_{zz} independent of $\omega_c\tau$, but at the maxima the integral in Eq. (4) of the sinusoidal v_z and the exponential factor means σ_{zz} decreases with increasing $\omega_c\tau$ for $\omega_c\tau \gg 1$ (see Appendix D). This means the AMRO peaks increase with B and τ , as seen. Magnetoresistance oscillations are often plotted against $\omega_c\tau$ itself^{12,30}; in this work, the dependences on the magnetic field and the scattering time are considered separately, to show that both parameters have an effect and to enable direct comparison with previous work in which these parameters are considered individually^{15,18}. The variation of the simulated AMRO with the strength of the magnetic field is similar to that measured experimentally on PdCoO₂ in Ref. 15, and also strongly resemble those calculated in Ref. 15, which have an almost sinusoidal curve with a 60° periodicity in ϕ . The best correspondence between the AMRO of this work and Ref. 15 is for low values of $k_{1,3} = 0.005 - 0.01 \text{ \AA}^{-1}$, somewhat larger than the experimental value of 0.001 \AA^{-1} extracted from quantum oscillations¹⁹.

B. The angular magnetoresistance oscillations due to out-of-plane rotation

The most common way of using AMRO to extract information about the Fermi surface shape is looking at the effect as a function of the rotation of the magnetic field out of the (ab) -plane, from $\theta = 0$ ($B \parallel c$) to close to $\theta = 90^\circ$ ($B \perp c$), as a function of the magnetic field strength, B , and the degree of c -axis warping, $k_{1,3}$, as shown in Fig. 3. We observe that the magnitude of the AMRO peaks increases with increasing magnetic field, as would be expected from Eq. (6), as the quasiparticle are able to move further around their orbits before scattering, as mentioned previously. For a cylindrical Fermi surface with no warping, the peaks in magnetoresistance have the largest amplitude at higher θ angles (see Fig. 3a), as observed for experiments and calculations in other systems, due to the contribution of closed orbits to the magnetoresistance^{3,9,10}. When the c -axis warping, $k_{1,3}$, increases, we observe that the peaks closest to $\theta = 0^\circ$ begin to appear and to grow, dominating over the standard AMRO peaks visible at higher angles. These features show similarities to those observed experimentally for hexagonal PdCoO₂ and PtCoO₂^{18,31}, although they are at lower values of θ than the AMRO observed in other materials³, where the approximation $\mu \gg 1$ will no longer hold. As the warping increases, the central peaks move toward $\theta = 0$ (for $\phi = 0$) whilst these other peaks move outwards, towards even higher θ , as shown in Fig. 3a)-c). The movement of these peaks can be explained

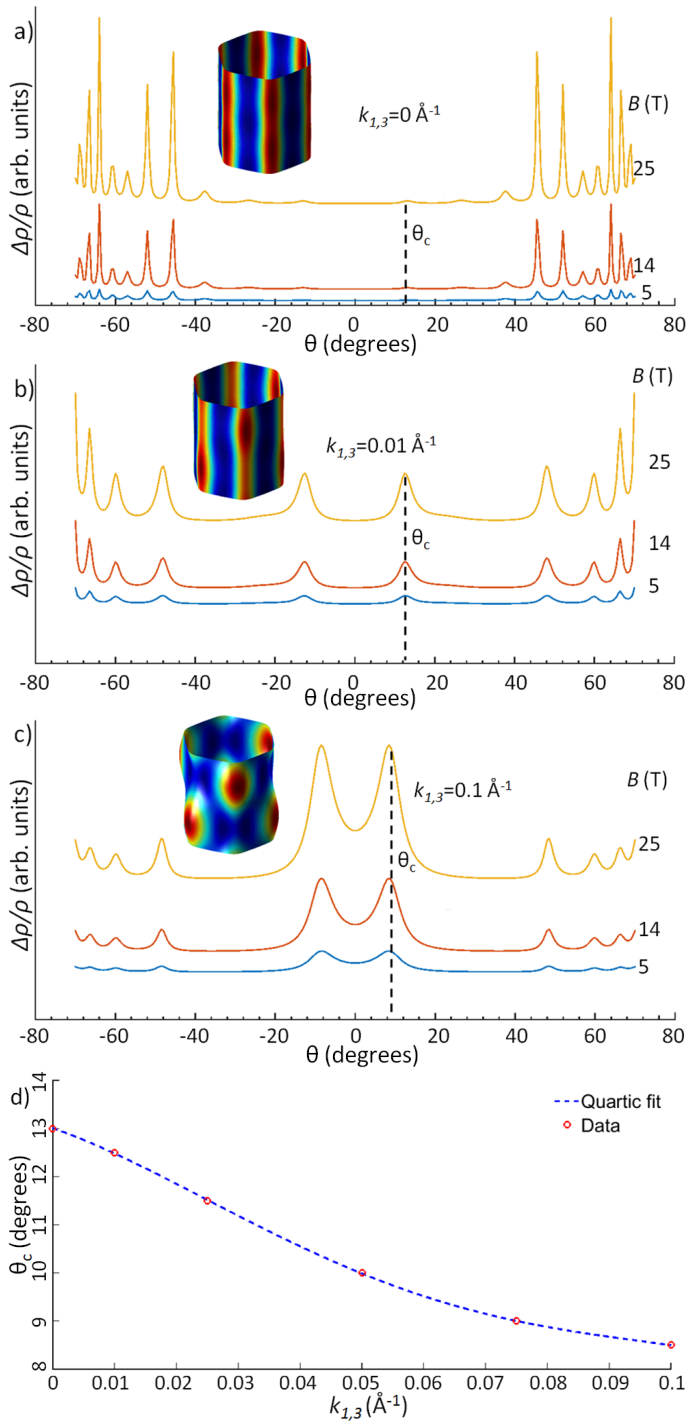


FIG. 3. (colour online) Simulated AMROs as a function of polar angle, θ , for at fixed magnetic field strengths, $B=5, 14, 25$ T, and different values of the degree of c -axis warping, $k_{1,3}$, as follows: a) 0, b) 0.01 and c) 0.1 \AA^{-1} , respectively and $\phi = 0^\circ$, $\tau = 10\text{ps}$ and $m^* = 1.5m_e$. Insets show the corresponding FS coloured by Fermi velocity, given by Eq. (2) and the vertical dashed line indicates the position of the dominant central peak at an angle θ_c . The variation of θ_c with $k_{1,3}$, is shown in d). The dotted line is a quartic fit of the form $ak_{1,3}^4 + bk_{1,3}^3 + ck_{1,3}^2 + dk_{1,3} + e$, with $a = -69302 \text{ \AA}^4$, $b = 16639 \text{ \AA}^3$, $c = -977.66 \text{ \AA}^2$, $d = -44.406 \text{ \AA}$ and $e = 13.007$.

by considering Yamaji angles²⁴ - certain values of θ at which all quasiparticle orbits have the same area. It can be shown that the average value of v_z around a quasiparticle orbit is proportional to the derivative of the orbit's area with respect to the k_z position of the orbit⁴. For Yamaji angles the orbit area is a constant, so v_z averages to zero, giving a minimum in σ_{zz} and thus a maximum in ρ_{zz} ^{6,29}. As the shape of the Fermi surface changes, so too do the Yamaji angles at which the AMRO peaks occur, as seen. The position of the central peaks, θ_c , changes slightly as the c -axis warping changes, and it seems to start to plateau as $k_{1,3}$ becomes large (see Fig. 2d). This decay is fitted to a quartic function, which could then be used to estimate the position of the central peaks for a given c -axis warping and ϕ .

We extend the above AMRO simulations to include the effect of changing the azimuthal angle of the magnetic field direction, ϕ , which is necessary to explore the shape of the Fermi surface. Fig. 4a) and d) show the simulated AMRO as a function of θ for various values of ϕ at fixed magnetic field $B = 25$ T and for two different values of $k_{1,3} = 0.01$ and 0.1 \AA^{-1} , respectively. A clear 60° periodicity in ϕ can be observed in both graphs by comparing the results from 0° up to 30° to those from 60° up to 90° , as would be expected due to the periodicity of the FS itself. The amplitude of the AMRO peaks, especially the central ones, as a function of ϕ is strongly sensitive to the exact value of $k_{1,3}$, being strongest near $\phi = 0^\circ$, and weakest near $\phi = 30^\circ$ in Fig. 4 (which are very similar to those for no warping in Fig. 3a). Based on Eq. (2), the c -axis warping reaches its maximum and minimum magnitude respectively at these ϕ points, which results in the AMROs being maximally and minimally different from the zero warping case. At high θ values approaching $\theta = 90^\circ$, the sharp AMROs become more tightly spaced and generally larger in amplitude as $k_{1,3}$ decreases (although there are some peaks that actually decrease in magnitude), and also strongly change their positions as a function of ϕ , especially for higher warping, as shown in Fig. 4e).

Extracting the shape of the Fermi surface from angle dependent magnetoresistance oscillation data is done by considering the values of θ at the maximum peaks in resistivity. It can be shown that as the magnetic field is rotated from the c -axis to the (ab) -plane, the position of peaks in the magnetoresistance can be linked to k_{\parallel} , the *maximum* projection of a Fermi wavevector onto the plane defined by the rotation of \mathbf{B} ^{4,24,28}. This allows us to extract the shape of the FS as we rotate the direction of the magnetic field, and thus the direction of the projected vector, in the (ab) -plane⁴. This is the core method behind using AMRO to map out Fermi surfaces, which is described in detail in the Appendices.

Fig. 4b) and e) show the variation with ϕ of the maximum possible projection of an in-plane Fermi wavevector onto the plane of rotation, k_{\parallel} , as extracted by fitting simulated data to the Yamaji angle formula (Eq. (40) in Appendices), for $k_{1,3}=0.01$ and 0.1 \AA^{-1} , respectively. In general, when $\tan \theta_n$ is plotted against $n \pm \frac{1}{4}$, the points fit well to a straight line, giving a reliable value of k_{\parallel} , as shown in Fig. 7 in the Appendices. The central peaks are almost always just off this line, as would be expected due to the breakdown of the approxima-

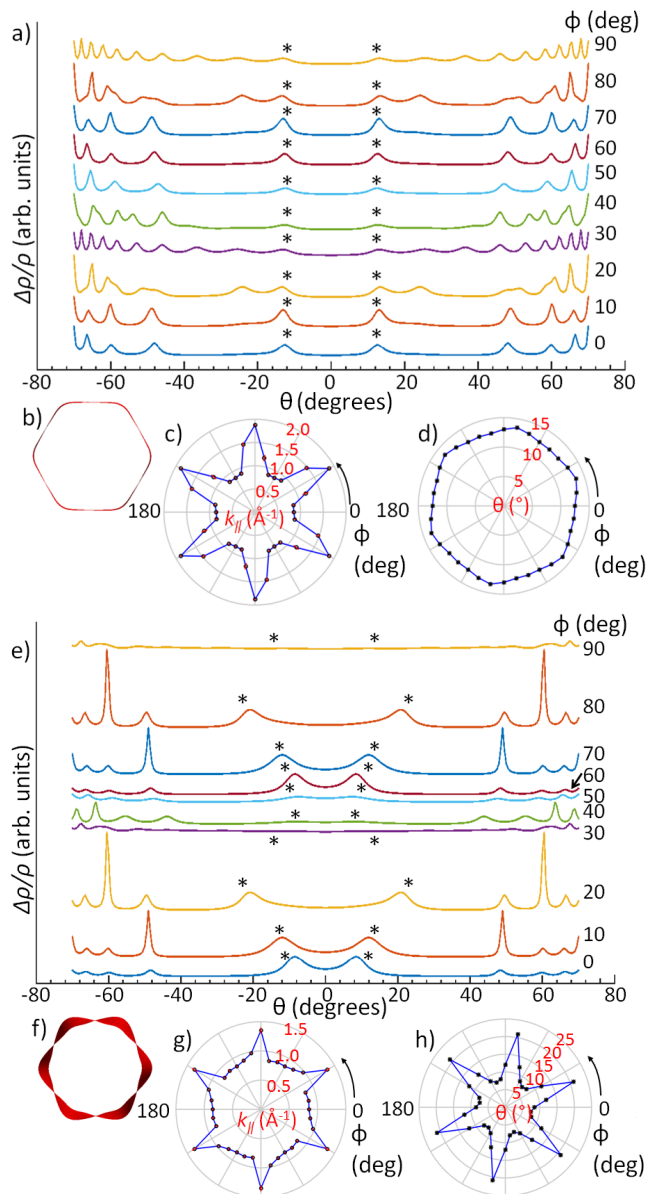


FIG. 4. (colour online) The simulated AMROs as a function of θ for given values of the azimuthal angle ϕ , and two different c -axis warping a) $k_{1,3} = 0.01 \text{ \AA}^{-1}$ and e) 0.1 \AA^{-1} corresponding to the Fermi surfaces shown as a top-down views in b) and f), respectively and using $B = 25 \text{ T}$, $\tau = 10 \text{ ps}$ and $m^* = 1.5 m_e$. The polar plots of $k_{||}$, against azimuthal angle ϕ (extracted as detailed in Appendix G) is shown in c) for $k_{1,3} = 0.01$ and g) for $k_{1,3} = 0.1 \text{ \AA}^{-1}$, respectively and the error bars are shown in red. The position of the central peaks, θ_c , is marked with asterisks and its variation with ϕ for each value of $k_{1,3}$ is shown separately in d) and h), respectively.

tion that $\mu \gg 1$, meaning that the formula $\mu = n\pi + \frac{\pi}{2} \pm \frac{\pi}{4}$ is no longer a good fit to the positions of the peaks. In the case of $30^\circ, 90^\circ$, etc., the central peaks have disappeared. If the central peaks are included when fitting for $k_{||}$, the error in the fitted gradient increases by an order of magnitude, but the fit is indistinguishable from the fit without the central peaks included. The polar plots of the $k_{||}$ shows a 60° periodicity

in ϕ , as expected from the periodicity in AMROs and the lattice in Fig. 4b) and e) and these shapes are different from the in-plane shape of the hexagonal Fermi surface, as the locus of $k_{||}$ does not have to match the outline of the FS, as seen previously for organic conducting salts^{3,4}. Furthermore, the variation of the position of the central peaks, θ_c , with ϕ , shown in Fig. 4c) and f) also has a 60° periodicity and for small warping is quite similar to the in-plane shape of the hexagonal Fermi surface. As the degree of warping increases, the range of θ_c values becomes much larger, shifting from around 1° for $k_{1,3} = 0.01 \text{ \AA}^{-1}$ to around 15° for $k_{1,3} = 0.1 \text{ \AA}^{-1}$.

Even for simple Fermi surfaces, the locus of $k_{||}$ may have a complicated shape, which makes it difficult to find an appropriate functional form. In the case of a simple ellipse⁴, the locus is a more complicated dumbbell-like shape, and for more complex Fermi surfaces, we may expect even more complex loci for $k_{||}$. Using this to trace out the shape of the Fermi surface is not a trivial task, becoming more difficult for higher degrees of warping, as is the case in the simulations presented here. These simulations of the polar plots of $k_{||}$ together with those of the raw AMRO data in Figs. 3 and 4, can be compared to future experimental results to identify the relevant parameters related to the Fermi surface in layered hexagonal materials.

Finally, we simulate AMROs for the Fermi surface of PdCo_2 , calculated based on quantum oscillation data¹⁹ (although we do not including the $k_{0,1}$ term), as shown in Fig. 5a), with ϕ taken as 55° in order to best match the positions of AMRO peaks observed experimentally in Ref.18. In order to find a better description for the available experimental data, we can vary both $k_{1,3}$ and ϕ and calculate the AMRO for each set of values, while minimizing the sum of the squares of the differences between the calculated and experimental peak positions. We find the best match for $k_{1,3} = 0.018 \text{ \AA}^{-1}$ and $\phi = 40^\circ$, shown in Fig. 5b). This estimate for $k_{1,3}$ is significantly larger than that measured through quantum oscillations¹⁹, and slightly outside the range estimated using the in-plane AMRO. In order to constrain the large number of available parameters in simulations and to better match simulation with experiment, a complete experimental data set is needed. Furthermore, the effects neglected in our calculation, such as anisotropy in the scattering time τ or the effective mass m^* , may also need to be taken into account in future work, and to obtain the sharp AMRO calculated here, the scattering time needs to be $\tau \gtrsim 0.5 \text{ ps}$, giving a rough guide to the quality of single crystals required for these studies. Despite such considerations, we would expect that certain features in our calculations will be robust measures of Fermi surface topography. In particular the central AMRO peaks are a very robust measure of interplane warping which may be little affected by the inclusion of anisotropy in τ and m^* ²³. Following their behaviour as a function of ϕ would allow the level of warping and the Fermi surface topography of materials with hexagonal lattices to be identified.

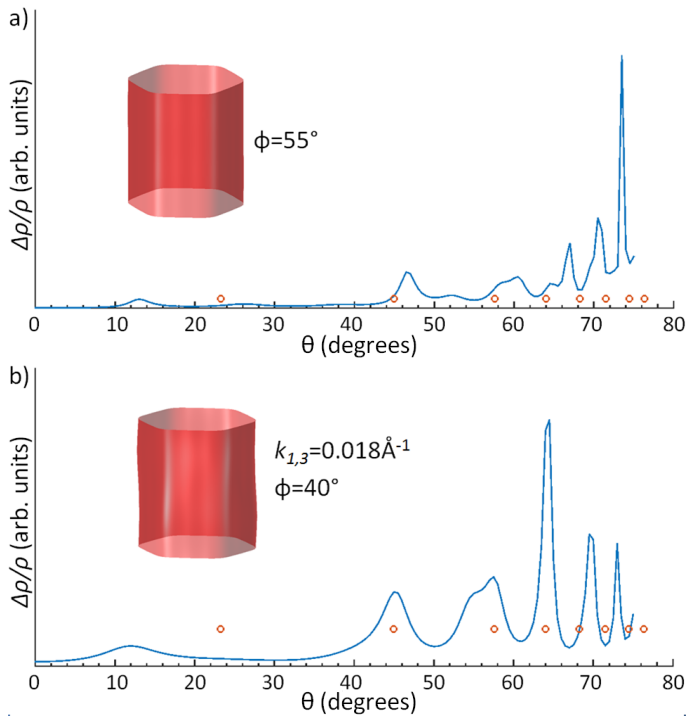


FIG. 5. (colour online) a) Simulated AMROs for a realistic Fermi surface of PdCoO₂ using $\phi = 55^\circ$ and $k_{0,0} = 0.9559$, $k_{0,6} = 0.04$, $k_{0,12} = 0.007$ and $k_{2,0} = -0.0025$ and $k_{1,3} = 0.001$ (in units of \AA^{-1}), as determined from quantum oscillations¹⁹. b) Simulated AMROs for $k_{1,3} = 0.018 \text{\AA}^{-1}$, $\phi = 40^\circ$ to best match the positions of the AMRO peaks measured for PdCoO₂ in Ref.18. The positions of the experimental AMRO peaks are marked by red circles and the other parameters used in simulations were $B = 25\text{T}$, $\tau = 10\text{ps}$ and $m^* = 1.5m_e$. A complete experimental angular dependence in (θ, ϕ) is necessary to constrain the large range of parameters.

IV. SUMMARY

In summary, we have investigated the angle dependent magnetoresistance oscillations corresponding to Fermi surfaces of structures with hexagonal lattices using a tight-binding expansion of the Fermi surface in terms of cylindrical harmonics. We have investigated the effect of varying degrees of c -axis warping as a function both of in-plane and out-of-plane rotations in magnetic field and found that the form of the AMRO is very sensitive to the degree of the c -axis warping. We also find that the dependence of the out-of-plane AMRO peak positions on the azimuthal angle ϕ becomes stronger for a more warped Fermi surface. We also attempt to compare our simulations to experimental work on a candidate compound, PdCoO₂^{15,18}. A further extension of this work could include the effect of anisotropy in the scattering time and effective mass. In general these quantities will depend on the position of the particle in reciprocal space, but their functional form must obey the symmetries of the Fermi surface. Finally, these simulations will be of great use to compare with future comprehensive experimental work on PdCoO₂, PtCoO₂ and similar compounds, in order to fully extract the topology of their Fermi surfaces from angle dependent magnetoresistance oscillations.

V. ACKNOWLEDGEMENTS

We thank Stephen Blundell for detailed and useful comments on our manuscript. We would like to acknowledge the use of the University of Oxford Advanced Research Computing (ARC) facility in carrying out this work. This work was mainly supported by EPSRC (EP/L001772/1, EP/I004475/1, EP/I017836/1). AIC acknowledges an EPSRC Career Acceleration Fellowship (EP/I004475/1).

¹ A. Damascelli, "Probing the electronic structure of complex systems by ARPES," *Physica Scripta* **2004**, 61 (2004).
² N. W. Ashcroft and N. D. Mermin, *Solid State Physics* (Cengage Learning, Belmont, 1976).
³ P. A. Goddard, S. J. Blundell, J. Singleton, R. D. McDonald, A. Ardavan, A. Narduzzo, J. A. Schlueter, A. M. Kini, and T. Sasaki, "Angle-dependent magnetoresistance of the layered organic superconductor $\kappa - (\text{ET})_2\text{Cu}(\text{NCS})_2$: simulation and experiment," *Phys. Rev. B* **69**, 174509 (2004).
⁴ J. Singleton, "Studies of quasi-two-dimensional organic conductors based on BEDT-TTF using high magnetic fields," *Reports on Progress in Physics* **63**, 1111 (2000).
⁵ K. Enomoto, S. Uji, T. Yamaguchi, T. Terashima, T. Konoike, M. Nishimura, T. Enoki, M. Suzuki, and I. S. Suzuki, "Fermi surface and interlayer transport in high-stage MoCl₅ graphite intercalation compounds," *Phys. Rev. B* **73**, 045115 (2006).
⁶ C. Bergemann, A. P. Mackenzie, S. R. Julian, D. Forsythe, and E. Ohmichi, "Quasi-two-dimensional Fermi liquid properties of the unconventional superconductor Sr₂RuO₄," *Adv. Phys.* **52**, 639 (2003).

⁷ M. Kimata, T. Terashima, N. Kurita, H. Satsukawa, A. Harada, K. Kodama, A. Sato, M. Imai, K. Kihou, C. H. Lee, H. Kito, H. Eisaki, A. Iyo, T. Saito, H. Fukazawa, Y. Kohori, H. Harima, and S. Uji, "Quasi-two-dimensional Fermi surfaces and coherent interlayer transport in KFe₂As₂," *Phys. Rev. Lett.* **105**, 246403 (2010).
⁸ M. Abdel-Jawad, M. P. Kennett, L. Balicas, A. Carrington, A. P. Mackenzie, R. H. McKenzie, and N. E. Hussey, "Anisotropic scattering and anomalous normal-state transport in a high-temperature superconductor," *Nat. Phys.* **2**, 821–825 (2006).
⁹ N. E. Hussey, M. Abdel-Jawad, A. Carrington, A. P. Mackenzie, and L. Balicas, "A coherent three-dimensional Fermi surface in a high-transition-temperature superconductor," *Nature* **425**, 814 (2003).
¹⁰ J. G. Analytis, M. Abdel-Jawad, L. Balicas, M. M. J. French, and N. E. Hussey, "Angle-dependent magnetoresistance measurements in Tl₂Ba₂CuO_{6+δ} and the need for anisotropic scattering," *Phys. Rev. B* **76**, 104523 (2007).
¹¹ W. Kang and O.-H. Chung, "Quasi-one-dimensional Fermi surface of (TMTSF)₂NO₃," *Phys. Rev. B* **79**, 045115 (2009).

- ¹² S. K. Lewin and J. G. Analytis, “Angle-dependent magnetoresistance oscillations of cuprate superconductors in a model with Fermi surface reconstruction and magnetic breakdown,” *Phys. Rev. B* **92**, 195130 (2015).
- ¹³ A. Nowojewski, P. A. Goddard, and S. J. Blundell, “Effect of magnetic breakdown on angle-dependent magnetoresistance in a quasi-two-dimensional metal: An analytically solvable model,” *Phys. Rev. B* **77**, 012402 (2008).
- ¹⁴ A. Nowojewski and S. J. Blundell, “Analytical treatment of in-plane magnetotransport in the Falicov-Sievert model,” *Phys. Rev. B* **82**, 075121 (2010).
- ¹⁵ H. Takatsu, J. J. Ishikawa, S. Yonezawa, H. Yoshino, T. Shishidou, T. Oguchi, K. Murata, and Y. Maeno, “Extremely large magnetoresistance in the nonmagnetic metal PdCoO₂,” *Phys. Rev. Lett.* **111**, 056601 (2013).
- ¹⁶ K. P. Ong, D. J. Singh, and P. Wu, “Unusual transport and strongly anisotropic thermopower in PtCoO₂ and PdCoO₂,” *Phys. Rev. Lett.* **104**, 176601 (2010).
- ¹⁷ V. Eyert, R. Frésard, and A. Maignan, “On the metallic conductivity of the delafossites PdCoO₂ and PtCoO₂,” *Chem. Mater.* **20**, 2370 (2008).
- ¹⁸ N. Kikugawa, P. Goswami, A. Kiswandhi, E. S. Choi, D. Graf, R. E. Baumbach, J. S. Brooks, K. Sugii, Y. Iida, M. Nishio, S. Uji, T. Terashima, P. M. C. Rourke, N. E. Hussey, H. Takatsu, S. Yonezawa, Y. Maeno, and L. Balicas, “Inter-planar coupling dependent magnetoresistivity in high purity layered metals,” arXiv:1412.5168v3 (2015).
- ¹⁹ C. W. Hicks, A. S. Gibbs, A. P. Mackenzie, H. Takatsu, Y. Maeno, and E. A. Yelland, “Quantum oscillations and high carrier mobility in the delafossite PdCoO₂,” *Phys. Rev. Lett.* **109**, 116401 (2012).
- ²⁰ J.M. Ziman, *Principles of the Theory of Solids, 2nd ed.* (Cambridge University Press, Cambridge, 1979).
- ²¹ P. D. Grigoriev, “Angular dependence of the Fermi surface cross-section area and magnetoresistance in quasi-two-dimensional metals,” *Phys. Rev. B* **81** (2010).
- ²² MATLAB, *version 8.4 (R2014b)* (The MathWorks Inc., Natick, Massachusetts, 2014).
- ²³ M. P. Kennett and R. H. McKenzie, “Sensitivity of the interlayer magnetoresistance of layered metals to intralayer anisotropies,” *Phys. Rev. B* **76**, 054515 (2007).
- ²⁴ K. Yamaji, “On the angle dependence of the magnetoresistance in quasi-two-dimensional organic superconductors,” *J. Phys. Soc. Jpn.* **58**, 1520 (1989).
- ²⁵ W. Shockley, “Effect of Magnetic Fields on Conduction “Tube Integrals”,” *Phys. Rev.* **79**, 191–192 (1950).
- ²⁶ R. G. Chambers, “The Kinetic Formulation of Conduction Problems,” *Proc. Phys. Soc. A* **65**, 458 (1952).
- ²⁷ S. J. Blundell, A. Ardavan, and J. Singleton, “Harmonics of the real-space velocity in cyclotron resonance experiments on organic metals,” *Phys. Rev. B* **55**, R6129–R6132 (1997).
- ²⁸ R. H. McKenzie and P. Moses, “Incoherent interlayer transport and angular-dependent magnetoresistance oscillations in layered metals,” *Phys. Rev. Lett.* **81**, 4492 (1998).
- ²⁹ R. Yagi, Y. Iye, T. Osada, and S. Kagoshima, “Semiclassical interpretation of the angular-dependent oscillatory magnetoresistance in quasi-two-dimensional systems,” *J. Phys. Soc. Jpn.* **59**, 3069–3072 (1990).
- ³⁰ V. M. Yakovenko and B. K. Cooper, “Angular magnetoresistance oscillations in bilayers in tilted magnetic fields,” *Physica E* **34**, 128–131 (2006).
- ³¹ P. Kushwaha, P. J. W. Moll, N. Nandi, and A. P. Mackenzie, “Crystal growth, resistivity and Hall effect of the delafossite metal PtCoO₂,” arXiv:1411.6162 (2014).
- ³² A. J. Schofield and J. R. Cooper, “Quasilinear magnetoresistance in an almost two-dimensional band structure,” *Phys. Rev. B* **62**, 10779 (2000).
- ³³ M. Abramowitz and I. A. Stegun, *Handbook of Mathematical Functions with Formulas, Graphs, and Mathematical Tables* (Dover, New York, 1964).
- ³⁴ C. W. Hicks, A. S. Gibbs, A. P. Mackenzie, H. Takatsu, Y. Maeno, and E. A. Yelland, “Supplementary Material of ‘Quantum oscillations and high carrier mobility in the delafossite PdCoO₂’,” *Phys. Rev. Lett.* **109**, 116401 (2012).

VI. APPENDICES

A. Linearised Boltzmann transport equation

The oscillations in AMRO are semi-classical in nature, and are due to the formation of cyclotron orbits on the FS and the changing area enclosed by them, as shown by Yamaji²⁴. To be able to find the conductivity and thus the resistivity, we need an equation that describes the evolution of the quasiparticle distribution in our material semi-classically - the linearised Boltzmann transport equation²⁰. To arrive at this, firstly we define $f_{\mathbf{k}}(\mathbf{r})$ as the steady state distribution of charged fermions under the influence of scattering, diffusion and electromagnetic forces. We can then assert that

$$\frac{\partial f_{\mathbf{k}}}{\partial t}_{\text{total}} = \frac{\partial f_{\mathbf{k}}}{\partial t}_{\text{scattering}} + \frac{\partial f_{\mathbf{k}}}{\partial t}_{\text{diffusion}} + \frac{\partial f_{\mathbf{k}}}{\partial t}_{\text{EM forces}} = 0. \quad (7)$$

At constant temperature, we can neglect the diffusion term. The scattering term is approximated using the relaxation time approximation - we define $g_{\mathbf{k}} = f_{\mathbf{k}} - f_{\mathbf{k}}^0$, where $f_{\mathbf{k}}^0$ is the equilibrium distribution, and a scattering time τ , and write the scattering term as

$$\frac{\partial f_{\mathbf{k}}}{\partial t}_{\text{scattering}} = -\frac{g_{\mathbf{k}}}{\tau}. \quad (8)$$

The electromagnetic term is written as

$$\frac{\partial f_{\mathbf{k}}}{\partial t}_{\text{EM fields}} = \frac{\partial f_{\mathbf{k}}}{\partial \mathbf{k}} \frac{\partial \mathbf{k}}{\partial t} = -\frac{e}{\hbar} (\mathbf{E} + \mathbf{v} \times \mathbf{B}) \cdot \left(\frac{\partial g_{\mathbf{k}}}{\partial \mathbf{k}} + \frac{\partial f_{\mathbf{k}}^0}{\partial \mathbf{k}} \right). \quad (9)$$

Substituting these expressions into Eq. (7) and using $\frac{\partial f_{\mathbf{k}}^0}{\partial \mathbf{k}} = \frac{\partial f_{\mathbf{k}}^0}{\partial \varepsilon} \frac{\partial \varepsilon}{\partial \mathbf{k}} = \frac{\partial f_{\mathbf{k}}^0}{\partial \varepsilon} \hbar \mathbf{v}$, we get

$$-\frac{e}{\hbar} (\mathbf{E} + \mathbf{v} \times \mathbf{B}) \cdot \frac{\partial g_{\mathbf{k}}}{\partial \mathbf{k}} - e (\mathbf{E} + \mathbf{v} \times \mathbf{B}) \cdot \mathbf{v} \frac{\partial f_{\mathbf{k}}^0}{\partial \varepsilon} = \frac{g_{\mathbf{k}}}{\tau}. \quad (10)$$

Applying $\mathbf{v} \cdot (\mathbf{v} \times \mathbf{B}) = 0$ and neglecting the $\mathbf{E} \cdot \frac{\partial g_{\mathbf{k}}}{\partial \mathbf{k}}$, as it is a quadratic deviation from Ohm's Law and we wish to linearise the equation, we get

$$e \mathbf{E} \cdot \mathbf{v} \left(-\frac{\partial f_{\mathbf{k}}^0}{\partial \varepsilon} \right) = \frac{g_{\mathbf{k}}}{\tau} + \frac{e}{\hbar} (\mathbf{v} \times \mathbf{B}) \cdot \frac{\partial g_{\mathbf{k}}}{\partial \mathbf{k}}. \quad (11)$$

B. Shockley-Chambers tube integral

We now need to solve the linearised Boltzmann transport equation to obtain the conductivity as an integral equation. If we only have a magnetic field acting on the system, the Lorentz force is $\mathbf{F} = \frac{\partial \mathbf{k}}{\partial t} = -\frac{e}{\hbar} \mathbf{v} \times \mathbf{B}$. Substituting this into Eq. (3), and defining the phase angle round the orbit α as $d\alpha = \omega_c dt$, where $\omega_c = \frac{eB}{m^*}$, we obtain

$$e \mathbf{E} \cdot \mathbf{v} \left(-\frac{\partial f_{\mathbf{k}}^0}{\partial \varepsilon} \right) = \frac{g_{\mathbf{k}}}{\tau} + \omega_c \frac{\partial g_{\mathbf{k}}}{\partial \alpha}. \quad (12)$$

The right hand side of this equation can be written as $\omega_c e^{-\frac{\alpha}{\omega_c \tau}} \frac{\partial}{\partial \alpha} \left(e^{\frac{\alpha}{\omega_c \tau}} g_{\mathbf{k}} \right)$, allowing us to obtain (using Einstein summation notation):

$$\begin{aligned} g_{\mathbf{k}} &= \left(-\frac{\partial f_{\mathbf{k}}^0}{\partial \varepsilon} \right) e^{-\frac{\alpha}{\omega_c \tau}} \int_{-\infty}^{\alpha} \frac{e}{\omega_c} e^{\frac{\alpha'}{\omega_c \tau}} E_j v_j(\alpha') d\alpha' \\ &= \left(-\frac{\partial f_{\mathbf{k}}^0}{\partial \varepsilon} \right) \int_0^{\infty} \frac{e}{\omega_c} e^{\frac{\alpha''}{\omega_c \tau}} E_j v_j(\alpha - \alpha'') d\alpha''. \end{aligned} \quad (13)$$

Now we need an expression for $d^3 \mathbf{k}$ to complete the integration. If we define k_B as parallel to \mathbf{B} , k_{\perp} in the direction of increasing α and k_{\parallel} along the radius of the orbit, we can write $d^3 \mathbf{k} = dk_B dk_{\perp} dk_{\parallel}$. We can express dk_{\parallel} in terms of the tangential velocity v_{\perp} using $\frac{\partial \mathbf{k}}{\partial t} = \frac{e}{\hbar} \mathbf{v} \times \mathbf{B}$ and $d\alpha = \omega_c dt$:

$$dk_{\parallel} = \frac{e v_{\perp} B}{\hbar} dt = \frac{v_{\perp} m^*}{\hbar} d\alpha. \quad (14)$$

We can also write the differential of the energy as

$$d\varepsilon = \hbar \frac{1}{\hbar} \frac{\partial \varepsilon}{\partial k_{\perp}} dk_{\perp} = \hbar v_{\perp} dk_{\perp}. \quad (15)$$

Putting all of this together, we obtain the current density $J_i = \frac{1}{4\pi^3} \int e v_i g_{\mathbf{k}} d^3 \mathbf{k} = \sigma_{ij} E_j$ as

$$J_i = \frac{e}{4\pi^3} \int d\varepsilon \int dk_B \int d\alpha \frac{m^*}{\hbar^2} v_i(\alpha) g_{\mathbf{k}}. \quad (16)$$

Substituting in the expression for $g_{\mathbf{k}}$, and using the fact that, as $f_{\mathbf{k}}^0$ is the Fermi-Dirac distribution and $T \ll T_F \simeq 10^5$ K, $(-\frac{\partial f_{\mathbf{k}}^0}{\partial \varepsilon}) = \delta(\varepsilon - \varepsilon_F)$, we obtain

$$\begin{aligned} \sigma_{ij} &= \frac{e^2}{4\pi^3 \hbar^2} \int dk_B \int_0^{2\pi} d\alpha \int_0^{\infty} d\alpha'' \\ &\quad v_i(\alpha) v_j(\alpha - \alpha'') \frac{m^*}{\omega_c} e^{-\frac{\alpha''}{\omega_c \tau}}. \end{aligned} \quad (17)$$

This expression can be generalised to include open orbits, as shown in Eq. (5) in the main text, to give:

$$\sigma_{ij} = \frac{e^2}{4\pi^3} \int d^3 \mathbf{k} \left(-\frac{\partial f_{\mathbf{k}}^0}{\partial \varepsilon} \right) v_i(\mathbf{k}, 0) \int_{-\infty}^0 v_j(\mathbf{k}, t) e^{\frac{t}{\tau}} dt. \quad (18)$$

C. AMRO in-plane integral

From Eq. (5), one can obtain the equation (as in Ref. 32)

$$\sigma_{ij} = \frac{e^2}{4\pi^3} \oint \frac{dS}{\hbar |\mathbf{v}|} \int_0^{\infty} v_i(0) v_j(t) e^{-\frac{t}{\tau}} dt \quad (19)$$

where dS is an area element of the FS. We can neglect the small closed orbits that will form on the sides of the FS, as they will give a very small contribution to the conductivity. The velocities depend on time through k_z , which, if we take the z -component of the Lorentz force, is given by

$$\hbar \frac{dk_z}{dt} = -e v_F B \sin \theta \quad (20)$$

where $\theta = \mathbf{v} \wedge \mathbf{B} = \psi - \phi$. ψ is the azimuthal angle that will be integrated over, and ϕ is the azimuthal angle of the magnetic field. Making the approximation that $k_F \simeq k_{00}$, this equation is solved by $k_z(t) = -\frac{ek_{00}B}{m^*}t \sin \theta + k_z(0)$. $k_z(0)$ will be one of the variables of integration. $|\mathbf{v}| = v_F = \frac{\hbar}{m^*}k_F$, so putting all of this together, we obtain

$$\sigma_{ij} = \frac{e^2}{4\pi^3} \frac{m^*}{\hbar^2} \int_{-\frac{3\pi}{c}}^{\frac{3\pi}{c}} dk_z \int_0^{2\pi} d\psi \int_0^\infty dt \frac{v_i(0)v_j(t)e^{-\frac{t}{\tau}}}{k_F(0)}. \quad (21)$$

In order to compute this using MATLAB²², the variable change $x = k_z(t)$ was made, giving the integral

$$\sigma_{ij} = \frac{e^2}{4\pi^3} \frac{m^*}{\hbar^2} \int_{-\frac{3\pi}{c}}^{\frac{3\pi}{c}} dk_z \int_0^{2\pi} d\psi \int_{-\infty}^{k_z} dx \frac{v_i(k_z, \psi)v_j(x, \psi)}{\omega k_F(k_z, \psi)} e^{-\frac{k_z}{\omega\tau \sin \theta}} e^{\frac{x}{\omega\tau \sin \theta}} \quad (22)$$

where $\omega = \frac{ek_{00}B}{m^*}$.

D. AMRO out-of-plane integral

Starting from Eq. (4), we can project dk_B onto the c-axis, giving $dk_B = dk_0 \cos \theta$. In addition to this, we can imagine rotating the whole co-ordinate system by θ , and consider the orbit due to a field of B at angle θ to be due to a field of $B \cos \theta$ along the c -axis, as long as we still enter the correct value of k_z into k_F . This has the effect of taking $\omega_c \rightarrow \omega_c \cos \theta$, and $k_z = k_0 - k_F(k_0, \alpha) \cos \alpha \tan \theta$. Putting all of this together, we obtain the equation

$$\sigma_{ij} = \frac{e^2 m^*}{4\pi^3 \hbar^2 \omega_c} \int_{-\frac{3\pi}{c}}^{\frac{3\pi}{c}} dk_0 \int_0^{2\pi} d\alpha \int_0^\infty d\alpha'' e^{-\frac{\alpha''}{\omega_c \tau \cos \theta}} v_i(k_0 - k_F(k_0, \alpha + \phi) \cos \alpha \tan \theta, \alpha) v_j(k_0 - k_F(k_0, \alpha - \alpha'' + \phi) \cos(\alpha - \alpha'') \tan \theta, \alpha - \alpha''). \quad (23)$$

Now, we write the velocities as Fourier series^{10,27}, defined as

$$v_i(k_0 - k_F(k_0, \alpha) \cos \alpha \tan \theta, \alpha) = \sum_{n=0}^{\infty} a_n \cos n\alpha + b_n \sin n\alpha, \quad (24)$$

$$v_j(k_0 - k_F(k_0, \alpha - \alpha'') \cos(\alpha - \alpha'') \tan \theta, \alpha - \alpha'') = \sum_{n=0}^{\infty} c_n \cos n(\alpha - \alpha'') + d_n \sin n(\alpha - \alpha''). \quad (25)$$

We then expand out $\cos n(\alpha - \alpha'') = \cos n\alpha \cos n\alpha'' + \sin n\alpha \sin n\alpha''$ and $\sin n(\alpha - \alpha'') = \sin n\alpha \cos n\alpha'' - \cos n\alpha \sin n\alpha''$. The α'' integral can now be completed, using

$$\int_0^\infty \cos n\alpha'' e^{-\frac{\alpha''}{\omega_c \tau \cos \theta}} d\alpha'' = \frac{\omega_c \tau \cos \theta}{1 + (\omega_c \tau \cos \theta)^2 n^2}, \quad (26)$$

$$\int_0^\infty \sin n\alpha'' e^{-\frac{\alpha''}{\omega_c \tau \cos \theta}} d\alpha'' = \frac{n(\omega_c \tau \cos \theta)^2}{1 + (\omega_c \tau \cos \theta)^2 n^2}. \quad (27)$$

This leaves us with the integral

$$\sigma_{ij} = \frac{e^2 m^*}{4\pi^3 \hbar^2 \omega_c} \int_{-\frac{3\pi}{c}}^{\frac{3\pi}{c}} dk_0 \sum_{n,m=0}^{\infty} \int_0^{2\pi} d\alpha (a_m \cos m\alpha + b_m \sin m\alpha) \left(c_n \left[\frac{\omega_c \tau \cos \theta \cos n\alpha}{1 + (\omega_c \tau \cos \theta)^2 n^2} + \frac{n(\omega_c \tau \cos \theta)^2 \sin n\alpha}{1 + (\omega_c \tau \cos \theta)^2 n^2} \right] + d_n \left[\frac{\omega_c \tau \cos \theta \sin n\alpha}{1 + (\omega_c \tau \cos \theta)^2 n^2} - \frac{n(\omega_c \tau \cos \theta)^2 \cos n\alpha}{1 + (\omega_c \tau \cos \theta)^2 n^2} \right] \right). \quad (28)$$

Finally, we can complete the integrals over α by using (for m or $n \neq 0$):

$$\int_0^{2\pi} \cos m\alpha \cos n\alpha = \pi \delta_{mn}, \quad (29)$$

$$\int_0^{2\pi} \sin m\alpha \sin n\alpha = \pi \delta_{mn}, \quad (30)$$

$$\int_0^{2\pi} \sin m\alpha \cos n\alpha = 0, \quad (31)$$

and for $m, n = 0$

$$\int_0^{2\pi} \cos m\alpha \cos n\alpha = 2\pi, \quad (32)$$

$$\int_0^{2\pi} \sin m\alpha \sin n\alpha = 0. \quad (33)$$

This gives, finally, the equation

$$\sigma_{ij} = \frac{e^2}{4\pi^3 \hbar^2} \frac{m^*}{\omega_c} \int_{-\frac{3\pi}{c}}^{\frac{3\pi}{c}} dk_0 a_0 c_0 + \frac{1}{2} \sum_{n=1}^{\infty} \left[\frac{a_n c_n + b_n d_n}{1 + (\omega_c \tau_0 \cos \theta)^2 n^2} - \frac{(a_n d_n - b_n c_n) n \omega_c \tau_0 \cos \theta}{1 + (\omega_c \tau_0 \cos \theta)^2 n^2} \right]. \quad (34)$$

E. Velocities

The FS is effectively defined by an equation, in cylindrical co-ordinates, of the form $|\mathbf{k}| = f(\psi, k_z)$. The Fermi velocity is defined by $v_F = \frac{1}{\hbar} \frac{\partial \epsilon_F}{\partial \mathbf{k}} = \frac{\hbar k_F}{m^*} \frac{\partial k_F}{\partial \mathbf{k}}$. This means that the velocity is perpendicular to the FS at all times. Calculating the derivative, we find that the velocity is in the direction $\hat{\mathbf{k}} - \frac{1}{k_F} \frac{\partial k_F}{\partial \psi} \hat{\psi} - \frac{\partial k_F}{\partial k_z} \hat{\mathbf{k}}_z$. This tells us that $v_z = \frac{\hbar k_F}{m^*} \frac{\partial k_F}{\partial k_z}$, so the remaining velocity is given by $\sqrt{\left(\frac{\hbar k_F}{m^*}\right)^2 - v_z^2}$. If we then define the angle between the in-plane velocity and the x-axis as

γ (the angle between the radial direction and the x-axis is ψ), we can easily see that $\tan(\psi - \gamma) = -\frac{1}{k_F} \frac{\partial k_F}{\partial \psi}$. Rearranging this, we obtain $\gamma = \psi + \arctan\left(\frac{1}{k_F} \frac{\partial k_F}{\partial \psi}\right)$. It is then simple to see that

$$v_x = \cos \gamma \sqrt{\left(\frac{\hbar k_F}{m^*}\right)^2 - v_z^2}, \quad (35)$$

$$v_y = \sin \gamma \sqrt{\left(\frac{\hbar k_F}{m^*}\right)^2 - v_z^2}. \quad (36)$$

We can now take advantage of the fact that $\frac{1}{k_F} \frac{\partial k_F}{\partial \psi}$ is small (at maximum $\simeq 0.48$ for $k_{1,3} = 0.1 \text{ \AA}^{-1}$), allowing us to neglect it, making $\gamma \simeq \psi$. As $\frac{\partial k_F}{\partial k_z} \simeq k_{1,3} \ll 1$ at maximum for large $k_{1,3}$, v_z^2 is much less than $\left(\frac{\hbar k_F}{m^*}\right)^2$, allowing us to neglect it too, leading to the simple expressions

$$v_x = \cos \psi \frac{\hbar k_F}{m^*}, \quad (37)$$

$$v_y = \sin \psi \frac{\hbar k_F}{m^*}. \quad (38)$$

F. Full matrix and simplified methods of calculating AMRO

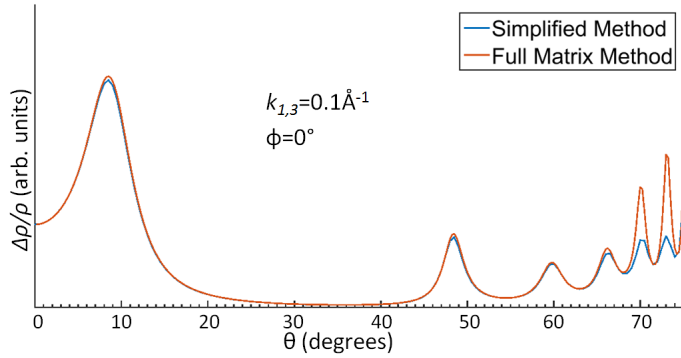


FIG. 6. (colour online) Simulated AMRO calculated using the full matrix method, where the entire conductivity matrix is calculated and then inverted to obtain ρ_{zz} , and the simplified method, where $\rho_{zz} = \frac{1}{\sigma_{zz}}$ is used. The positions of the peaks and form of the AMRO produced by the two methods agree very well, suggesting the less computationally expensive and error-prone simplified method can be used instead of the full matrix method. $k_{1,3} = 0.1 \text{ \AA}^{-1}$, $\phi = 0^\circ$, $\tau = 10 \text{ ps}$ and $B = 25 \text{ T}$ in both simulations.

G. Yamaji angles and mapping the FS

In order to map the FS using AMRO, we need a way of extracting k_{\parallel} from the data for different values of the azimuthal angle, ϕ . In this work the chosen parameters were

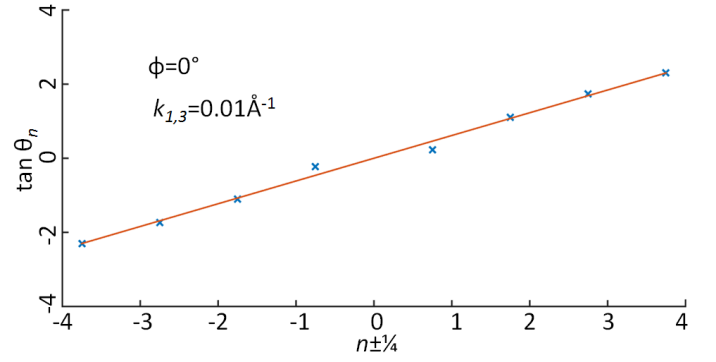


FIG. 7. (colour online) Fitting of AMRO peaks to the Yamaji angle formula, as shown in Eq. (40), for $k_{1,3} = 0.01 \text{ \AA}^{-1}$ and $\phi = 0^\circ$. The gradient of the line gives $k_{\parallel} = 0.851 \pm 0.006 \text{ \AA}^{-1}$. The central peaks (those with the smallest value of $|n \pm \frac{1}{4}|$) can clearly be seen to be slightly off the straight line defined by the other peaks, as would be expected due to the breakdown of the approximation that $\mu \gg 1$. The fit shown does not use the central peaks - if these peaks are included, the error in the gradient increases by an order of magnitude, but the line is indistinguishable from the fit shown.

$B = 25 \text{ T}$, $\tau = 10 \text{ ps}$, $m^* = 1.5 m_e$ and thus $\omega_c \tau$ is large enough to neglect terms other than $J_0(\mu)$ in the Bessel function sum. This implies we will get minima in σ_{zz} , and thus maxima in ρ_{zz} , at the zeros of $J_0(\mu)$. For $|\mu| \gg 1$, we can use the large argument expansion of the zeroth order Bessel function³³:

$$J_0(\mu) \simeq \sqrt{\frac{2}{\pi \mu}} \begin{cases} \cos\left(\mu - \frac{\pi}{4}\right) & \mu > 0 \\ \cos\left(\mu + \frac{\pi}{4}\right) & \mu < 0 \end{cases}. \quad (39)$$

This has zeros at $\mu = n\pi + \frac{\pi}{2} \pm \frac{\pi}{4}$, where $+$ is for $\mu < 0$ and $-$ is for $\mu > 0$. We can then index each of the peaks in the AMRO found with an integer n , so the θ value of the peak is given by θ_n . $n < 0$ if $\theta_n < 0$, and vice versa, and $|n|$ grows as $|\theta_n|$ grows. If we index the peaks in this way, the results above tell us that we should be able to plot $\tan \theta_n$ against $n \pm \frac{1}{4}$ and fit it to the equation

$$\frac{ck_{\parallel}}{3} \tan \theta_n = \pi\left(n \pm \frac{1}{4}\right) + C(\phi) \quad (40)$$

where the \pm signs are taken as described above, and $C(\phi)$ is a constant dependent on ϕ . This provides us with a way of extracting k_{\parallel} and mapping the FS, as required. By considering the orbits of electrons in magnetic field, we can explain the origin of these peaks. At certain values of θ , all orbits have the same area, resulting in the z-component of the velocity averaging to zero and therefore a peak in magnetoresistance. Yamaji showed that these special values of θ precisely correspond to the peaks already mentioned²⁴, and are thus often called Yamaji angles¹².

H. Simulation of AMROs for a tetragonal Fermi surface

To test the robustness of our approach we have also performed calculations for a layered tetragonal system,

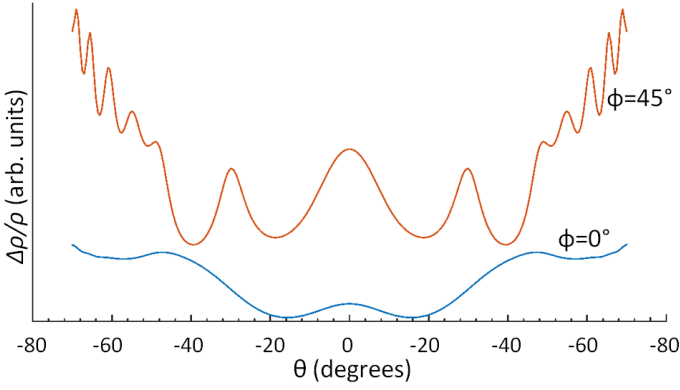


FIG. 8. (colour online) Calculated AMROs of a layered tetragonal material, with a FS similar to that of $\text{Ti}_2\text{Ba}_2\text{CuO}_{6+\delta}$: $k_F = k_{0,0} + k_{0,4} \cos 4\psi + k_{1,2} \cos \kappa \sin 2\psi + k_{1,6} \cos \kappa \sin 6\psi + k_{1,10} \cos \kappa \sin 10\psi$. Here $k_{0,0} = 0.729$, $k_{0,4} = -0.0219$, $k_{1,2} = 0.0031$, $k_{1,6} = 0.00217$ and $k_{1,10} = -0.00093 \text{ \AA}^{-1}$, with $B = 25 \text{ T}$, $\phi = 0^\circ$ and 45° , $\tau = 0.5 \text{ ps}$ and $m^* = 4.1m_e$, similar to previous work¹⁰.

$\text{Ti}_2\text{Ba}_2\text{CuO}_{6+\delta}$, shown in Fig. 8, which has strong AMRO features at low angles and agree qualitatively with available experiments¹⁰. This strengthens the generality of our method, its approximations and its applicability, which can be extended to other quasi-2D materials of various lattice symmetries.

I. Tight-binding model

The terms of the Fermi surface expansion used in this work, given by Eq. (2), can be linked to a tight-binding expansion involving both inter- and intra-plane nearest neighbour and next-nearest neighbour hopping terms^{15,34}. From a given tight-binding model and Fermi energy, a Fermi surface can be calculated that corresponds to that given by Eq. (2). Intra-plane next-nearest neighbour hopping as well as inter-plane hopping affect the value of $k_{1,3}$ in the expansion, whilst the values of the in-plane next-nearest neighbour transfer integral and the Fermi energy affect the overall hexagonal shape.

In previous tight-binding model calculations, the transfer integrals $t_{nn}, t_{nnn}, t_z, t_{zz}$ were given values of approximately 1.0, -0.23, 0.042, 0.011 eV, representing intra-plane nearest neighbour, in-plane next-nearest neighbour, inter-plane nearest neighbour and inter-plane next-nearest neighbour coupling respectively. The Fermi energy E_F was chosen as 0.22 eV³⁴. One possible tight-binding expression for the energy is of the form¹⁵

$$\begin{aligned} \varepsilon(\mathbf{k}) = & -2t_{nn}\{\cos(\mathbf{k} \cdot \mathbf{a}) + \cos(\mathbf{k} \cdot \mathbf{b}) + \cos(-\mathbf{k} \cdot (\mathbf{a} + \mathbf{b}))\} \\ & - \frac{2t_{zz}}{3} \cos(\mathbf{k} \cdot \mathbf{c}) - \sqrt{3}t_{nnn}\{\cos^2(\mathbf{k} \cdot \mathbf{a}) + \cos^2(\mathbf{k} \cdot \mathbf{b}) \\ & + \cos^2(-\mathbf{k} \cdot (\mathbf{a} + \mathbf{b}))\}. \end{aligned} \quad (41)$$

Although using a tight-binding model gives access to more information than simply the geometry of the Fermi surface, we choose to work directly from the Fermi surface expansion because it gives more direct insight into what is actually observed experimentally - the shape of the Fermi surface itself⁶.

J. Symmetry operations

The symmetry operations used to construct the Fermi surface expansion in Section II can be described more intuitively in Cartesian co-ordinates as follows:

1. A screw symmetry, composed of a rotation about the origin by 60° and a translation in the z -direction by half a reciprocal lattice vector.
2. A rotation symmetry about the origin by 120° .
3. Inversion through the origin.
4. Reflection in the plane $x = 0$.
5. Reflection in the plane $y = \sqrt{3}x$, i.e. a line at a 60° angle to the x -axis.

The screw symmetry is responsible for the lack of a $k_{0,1}$ term, present in Ref. 19, in the Fermi surface expansion used in this work, which is given by Eq. (2).